Materials Physics and Mechanics 42 (2019) 165-177 Received: April 17, 2018

DENSIFICATION RATE INFLUENCE ON NANOPOWDER COMPACTIBILITY

G.Sh. Boltachev*, E.A. Chingina, A.V. Spirin, N.B. Volkov

Institute of Electrophysics, Ural Branch of RAS, Amundsen str. 106, Ekaterinburg, Russia

*e-mail: grey@iep.uran.ru

Abstract. The paper concerns processes of high-speed compaction of nanosized powders. The processes of uniform and uniaxial compaction have been simulated by the granular dynamics method. Nanoparticles interaction, in addition to known contact laws, includes dispersive attraction, formation of a strong interparticle bonding as well as the forces caused by viscous stresses in the contact region. For different densification rates, the densification curves (pressure vs. density) have been calculated. Relaxation of the stresses after the compression stage has been analyzed. The densification curves analysis allows us to suggest the dependence of compaction pressure as a function of strain rate in the form of $p \propto v^{1/8}$. The rate dependence obtained has been applied for interpretation of experimental data concerning high-speed processes of magnetic pulsed compaction of nanopowders.

Keywords: nanosized powders, granular dynamics method, high-speed compaction

1. Introduction

The nanopowder cold compaction is a very important stage of novel nanostructured materials production by the powder metallurgy [1,2]. As known, nanopowders in contrast to coarse-grained materials are very hard to densify due to the strong interparticle "friction", which is caused by the intense dispersion attraction, and agglomeration of particles [2,3,4]. To achieve a proper compact density for sintering the high quality, defect-free ceramic article, applying the high pressure of about several gigapascals is required. Such high pressures can even exceed the durability of pressing tools [2,3,5]. Thus, the theoretical description of powder body and reliable forecasting the compaction processes take on high topicality.

The present paper is devoted to development of theoretical description of oxide nanosized powders cold compaction processes [1,2] by taking into account the densification rate influence on the nanopowder compactibility. The microscopic study of nanopowders high-speed compaction processes is performed in the frameworks of the granular dynamics method [6,7]. This method is of interest due to the oxide nanoparticles, for example, produced by the method of wires electric explosion [8] or target laser evaporation [9], usually have high strength properties and a spherical form. Therefore, such powders are the most convenient object for simulations. Nowadays the granular dynamics method is extensively used for description of compaction processes of different micro- and nanopowders [6,7,10,11]. However quasistatic compaction processes are investigated as a rule. After every step of model cell deformation the new equilibrium locations of particles are determined during a large number of equilibration steps [6,7]. At the same time, in view of necessity to achieve extremely large compaction pressures the magnetic pulsed methods [2,5] attract a great attention. These methods allow increasing the pressure into compacts owing to the inertial effects. The relative rate of compact densification is here about 0.1 μs^{-1}. It is known that

http://dx.doi.org/10.18720/MPM.4222019_2

dynamical yield strength is not equal to static one. For example, the yield strength of metal at high-speed loading can exceed the static limit by several times [12-14]. Corresponding studies of the rate influence on the nanopowders compaction processes have not been conducted yet.

2. Details of the granular dynamics method

We simulate the dynamical processes of uniform and uniaxial pressing, which are characterized with the relative densification rate $v = (1/\rho)(d\rho/dt)$, where ρ is the density and t is the time, from value 10^1 μs^{-1} up to 10^4 μs^{-1}. Such high rates are caused by numerical troubles, i.e., the large times for simulations of small-rate processes. As can be seen below, the simulation results obtained are easy extrapolated to the region of smaller rates.

The model cell has a form of cube with volume $V_{cell} = L_{cell}^3$ in the case of uniform compaction processes and a form of rectangular parallelepiped with a base L_{cell}^2 and a height H_z along the direction of pressing in the case on uniaxial compaction. The density is implied as a relative volume of the model cell occupied by the particles, i.e., $\rho = N_p(\pi/6)d_g^3/V_{cell}$, where $N_p = 2000$ is the number of particles in the cell, d_g is the particle diameter. Periodic boundary conditions are used on all the sides of the cell. For initial packing generation, the algorithm defined in [6] is used, which allows us to create isotropic and uniform structures in a form of the connected 3D-periodic cluster. The initial density is $\rho_0 = 0.24$. The system deformation is performed by simultaneous changes of cell sizes (all sizes at uniform pressing or the value of H_z only at uniaxial pressing) and proportional rescaling of corresponding particles coordinates. The relative displacements and rotations of particles are determined by the usual equations

$$m\frac{d^2r}{dt^2} = f, \qquad J\frac{d^2\theta}{dt^2} = M, \tag{1}$$

where $m = (\pi/6)\rho_m d_g^3$ is the particle mass, ρ_m is the density of the particle material, f and M are the total force and torque caused by other particles, $J = md_g^2/10$ is the inertia moment, θ is the rotation angle. The Verlet algorithm [15] is applied for the numerical solve of Eq. (1).

The stress tensor σ_{ij} averaged over the model cell is calculated by the known expression [6,10,11]

$$\sigma_{ij} = \frac{-1}{V_{cell}}\sum_{k<l} f_i^{(k,l)} r_j^{(k,l)}, \tag{2}$$

where the summation is performed over all pairs of interacting particles (k, l); $f^{(k,l)}$ is the total force affecting the particle "k" from the particle "l"; $r^{(k,l)}$ is the vector connecting the centers of the particles. The particle interactions described in detail elsewhere [6,7] include the elastic repulsion (modified Hertz law), the "friction" forces (Cattaneo – Mindlin and Jäger laws), the dispersive attraction force (Hamaker's formula), and the contact elasticity of flexure because of strong interparticle bonding. Alumina is implied as the particle material for which, in particular, the Young modulus E is 382 GPa and the Poisson ratio ν is 0.25. Other parameters of interaction laws are close to the parameters of system II in Refs. [6,7], which imitates alumina nanopowders [16] with particle diameter d_g = 10 nm.

The high value of speed of modeled processes requires taking into account the viscous stresses in the vicinity of the contact area of particles. Using the similarity of Hooke's elastic law and the Navier – Stokes equations the authors of Ref. [17] obtained the rigorous solution of the problem on contact interaction of viscoelastic spheres. In general case the influence of the viscous stresses has a form [17,18]

$$f_{visc} = A\frac{df_e}{d\xi}\frac{d\xi}{dt}, \tag{3}$$

where f_{visc} is the total force of the viscous stresses, f_e is the elastic force, ξ is the variable, which describes the body deformation, and the coefficient A neglecting the bulk viscosity is described as:

$$A = \frac{\eta(1-\nu^2)(1-2\nu)}{3E\nu^2}. \tag{4}$$

The shear viscosity coefficient η is estimated [19] by the known data on ultrasound damping into alumina. The coefficient of damping [20] into the isotropic medium $\gamma_t = \eta\omega^2/(2\rho_m c_t^3)$, where ω and c_t are the frequency and speed of sound. Using the value $\gamma_t \cong 230$ dB/m at the frequency of $\omega/2\pi = 1.0$ GHz [21] the shear viscosity coefficient η for alumina of 0.001 Pa s was obtained.

Starting from Eq. (3) it is not difficult to write all expressions which describe the interactions of viscoelastic spherical particles. For example, for linearized tangential force of "friction" we have

$$\frac{f_t}{E} = c_m a\delta + Ac_m a\frac{d\delta}{dt}, \qquad c_m = \frac{4}{(2-\nu)(1+\nu)}, \tag{5}$$

where δ is the relative tangential displacement of contacting particles, $a = \sqrt{hd_g}/2$ is the contact spot radius, $h = d_g - r$ is the depth of particle overlapping.

The characteristic time, $T = \left[(\pi\rho_m d_g^2)/(6E)\right]^{1/2}$, which transforms Eqs. (1) to dimensionless form, is equal to 0.74×10^{-12} s for our systems. The reduced time step of the numerical solving the equations (1) is $h_t = 0.04\ T$.

3. Simulation results

With the purpose of statistical averaging we have performed 10 independent calculations for each compression rate. Figure 1 presents the time-dependent hydrostatic pressure $p = -\mathrm{Sp}(\sigma_{ij})$ averaged and typical calculation curves for uniform compaction process with the compression rate $v = 100$ μs^{-1}. It is helpful to note that the initial structures are being generated by the algorithm of Ref. [6], which places the neighboring particles at equilibrium distances when attraction compensates repulsion. However the algorithm requires a preliminary relaxation step. It is needed since the dispersion forces between further particles are not taken into account in the algorithm that results in slight fluctuations of particles in the initial structure. In order to extinguish the fluctuations, initially generated structure relaxes for 5 ns (see the inset in Fig. 1).

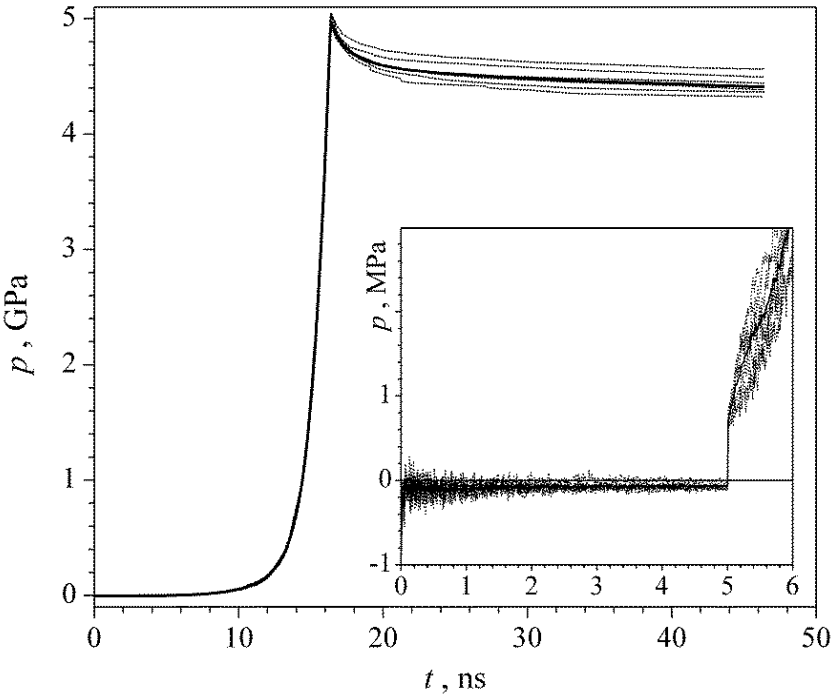

Fig. 1. Time dependence of pressure for the densification rate $v = 100$ μs^{-1}. Dotted lines are examples of calculation curves; solid line is the average over 10 independent calculations. Inset shows the period of the preliminary relaxation (5 ns) and the beginning of the compression

Compression of the model cell was performed up to the pressure p = 5 GPa for uniform pressing and up to the $p_z = -\sigma_{zz} = 5$ GPa for uniaxial pressing. After that the system was relaxed during 30 ns. A considerable reduction of stresses is observed at the relaxation stage after pressing. This reduction for the hydrostatic pressure (after uniform compaction) and for the pressure p_z (after uniaxial compaction) is well approximated by an expression

$$p(t) = p_0 + p_1 \exp\left(\frac{-t}{\tau_1}\right) + p_2 \exp\left(\frac{-t}{\tau_2}\right). \quad (6)$$

The numerical analysis has showed that post-compression relaxation proceeds in two stages: "rapid" with a characteristic time τ_1 of about tenths of nanoseconds, and "slow" with characteristic time of about τ_2 = 18 ns.

Figure 2 shows the total pressure drops after compaction processes, Δp, estimated by the approximations (6). The dependences of Δp on the compression rate are approximated as

$$\Delta p = (k_1 v)^{k_2}, \quad (7)$$

with parameters: k_1 = 0.020 μs, k_2 = 0.17 for the uniaxial process, and $k_1 = 7.4\times10^{-4}$ μs, k_2 = 0.19 for the uniform process. The extrapolation to the rate value of 0.1 μs^{-1} (see Fig. 2) gives $\Delta p \cong 350$ MPa for the uniaxial compaction, and 160 MPa for the uniform compaction. These values can be considered as preliminary estimates for the rate influence on the compaction curves at the processes of magnetic pulsed compaction [2,5].

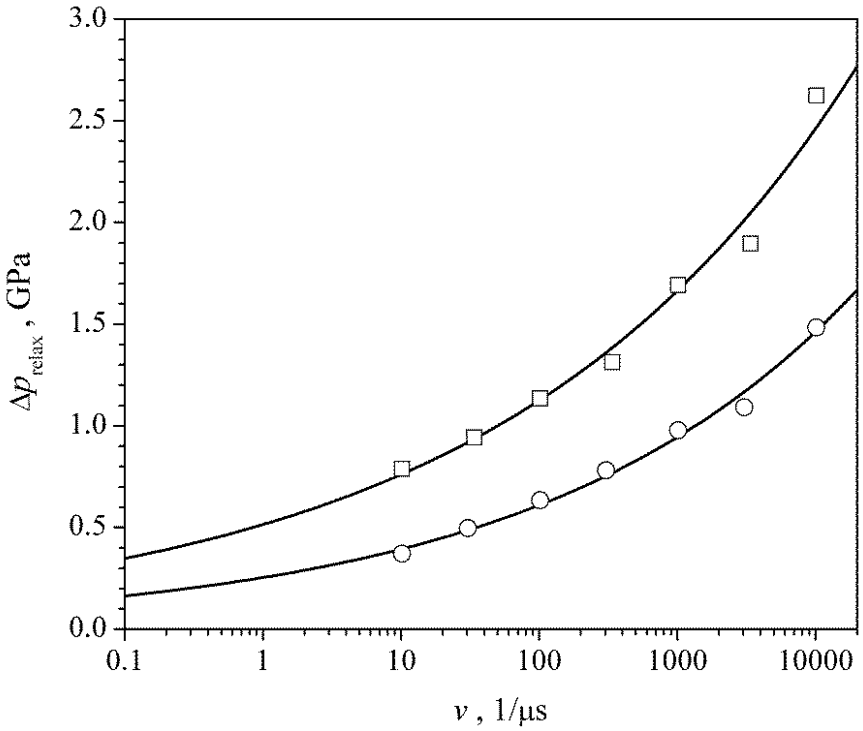

Fig. 2. Dependence of pressure drop at the stage of 30 ns relaxation after pressing on the compression rate for the uniform compaction (circles) and the uniaxial compaction (squares). Lines are the approximation of Eq. (7)

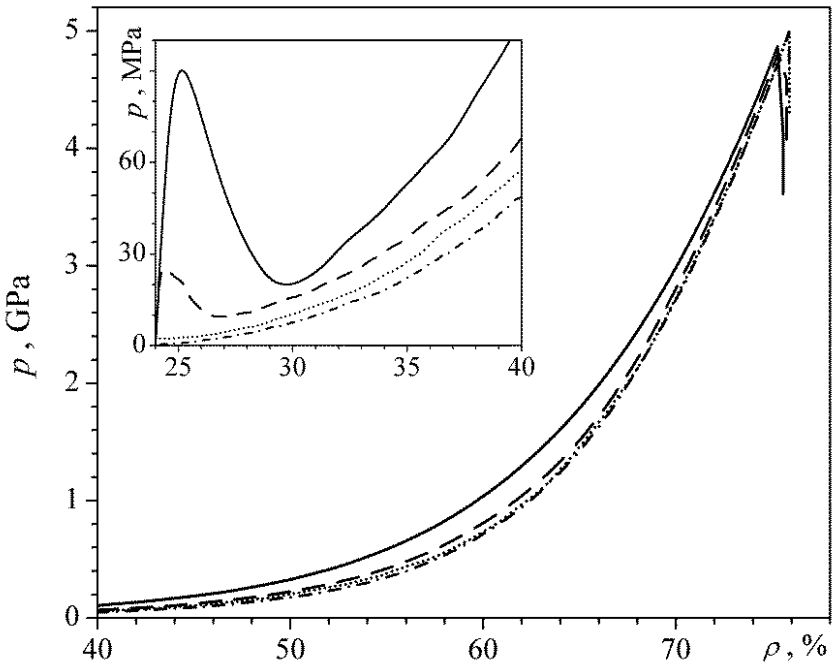

Fig. 3. Densification curves in "density – pressure" coordinates for strain rates v (in μs^{-1}): 10^4 (solid line), 3×10^3 (dashed line), 300 (dotted line), and 10 (dashed-dotted line). Inset shows the low pressure region

Figure 3 presents the compaction curves $p(\rho)$ for uniform compaction processes corresponding to the different densification rates. For uniaxial compaction processes the compaction curves $p_z(\rho)$ have a similar form. It is interesting that the $p(\rho)$ curves for large

rates has a local maximum at the beginning (see an inset in Fig. 3), which is very similar to the yield drop at stress-strain curves of metals [22]. At the densification rate $v = 10^4$ μs^{-1} the pressure at the maximum is achieved the values of 90 MPa for uniform pressing and 165 MPa for uniaxial pressing. This maximum has a dynamical nature and is caused by the retardation of relaxation processes from the powder compression. According to the simulation results, an increase in pressure up to the local maximum takes about 5 ps. This time is significantly less than the time of the "rapid" relaxation, which is about 50 ps in accordance with the analysis of relaxation stages after pressing (see Fig. 1). At slower densification rates, when $v < 300$ μs^{-1}, this maximum disappears.

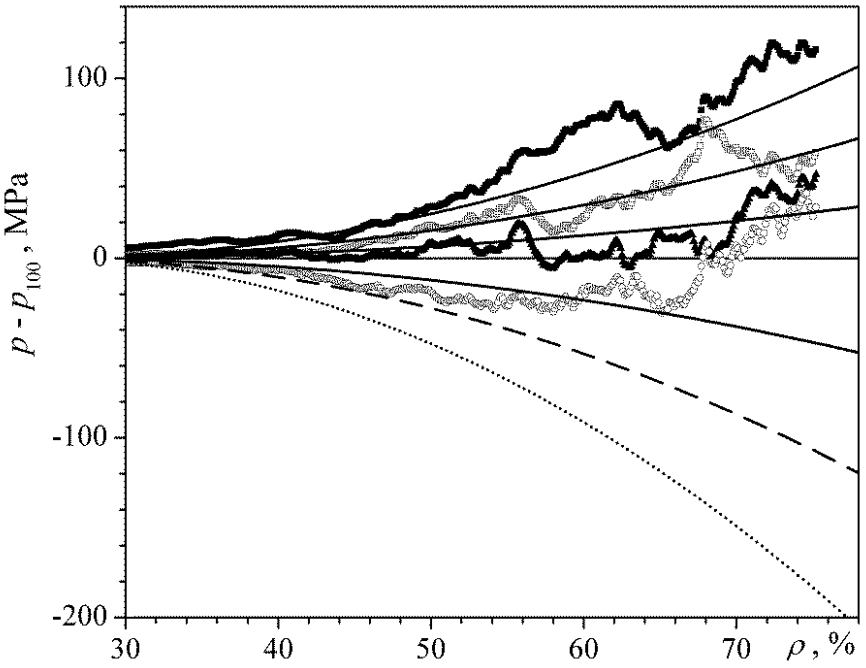

Fig. 4. The differences of compaction pressure from the pressure p_{100} corresponding to the rate $v = 100$ μs^{-1} as a function of density for the uniform pressing. Symbols are the simulation results for rates v (in μs^{-1}): 3000, 1000, 300, and 10 (from the top); smooth solid lines are the dependences of Eqs. (8), and (9) for the same rates; dashed line corresponds to the rate $v = 0.1$ μs^{-1}; dotted line is the static limit ($v = 0$)

To analyze the relative location of dependencies $p(\rho)$ (in the case of uniform pressing) and $p_z(\rho)$ (in the case of uniaxial pressing) the densification curves corresponding to the rate $v = 100$ μs^{-1} have been used as a reference one and the differences of compaction pressure corresponding other rates from the reference curve $p_{100}(\rho)$ have been analyzed. Figure 4 shows these differences for uniform compaction process. Taking into account a quite large statistical error of simulation results at the maximal density $\rho \cong 0.75$, where the pressure error comes up to 100 MPa, these differences are well approximated by the expression:

$$p(\rho, v) - p_{100}(\rho) = p_v(v)(\rho - \rho_0)^\gamma . \quad (8)$$

The analysis performed reveals that the index $\gamma \cong 2$. The strain-rate-dependent coefficient p_v is presented in Fig. 5. It can be seen that in the range of densification rates $v < 1000$ μs^{-1} the values p_v for uniform and uniaxial processes is well described by the common expression

$$p_v = p_{v0} + (k_v v)^{1/8}, \quad (9)$$

with parameters: $p_{v0} = -0.705$ GPa, $k_v = 5.7 \times 10^{-4}$ μs. As a result, passing on to the quasistatic conditions ($v \to 0$, the dotted line in Fig. 4) as a reference line ($p_{stat} = p_{100} + p_{v0}(\rho - \rho_0)^2$), we have obtained

$$p(\rho, v) = p_{stat}(\rho) + (k_v v)^{1/8}(\rho - \rho_0)^2 . \quad (10)$$

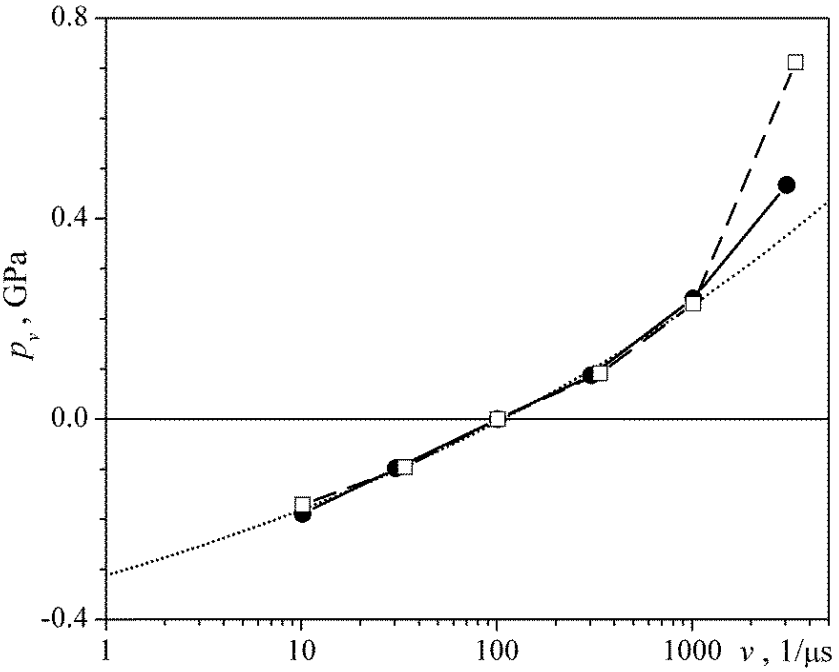

Fig. 5. The coefficient p_v of Eq. (8) as a function of strain rate. Squares are the simulation results for uniaxial compaction processes, circles are the simulation results for uniform compaction processes; dotted line is the common approximation of (9)

Figure 4 demonstrates the pressure differences corresponding to Eqs. (8)–(10). As a result, it can be seen that the pressure required for nanopowder compaction up to the density of $\rho \cong 0.75$, when using a dynamical process with rate about $v = 10^5$ s^{-1} (for example, magnetic pulsed methods), exceeds the pressure at a quasi-static compaction process by the value of about 80 MPa.

4. Experiments

In order to approve the relation (10) obtained within the granular dynamic method, two series of experiments on magnetic pulsed compaction (MPC) of alumina nanopowder were performed. Laboratory made Al_2O_3 nanopowder composed of δ and γ phases with average particle diameter $d_{BET} \cong 50$ nm was produced by electric explosion of aluminum wire. Theoretical density of material is $\rho_m \cong 3.66$ g/cm^3. The powder compaction was performed magnetically using cylindrical inductor as magnetic field source and copper shell (tube) as pressing mold (so-called θ-pinch mode, e.g. [2,23,24]). Two series of pulsed experiments (3 samples each) differed in the rate of external loading via the changing the magnetic field pulse duration. It was realized by using two inductors (tool coils): single-turn coil (inductor 1) and multi-turn coil (inductor 2), which were being connected to the capacitor battery (C = 425 μF). In both cases magnetic field amplitude was kept at the same value, about 25 T, by adjusting the charging voltage of the capacitor battery.

To densify the powder it was placed inside a mold consisted of an outer copper tube and a coaxially mounted rod of hard steel. Outer diameter, thickness, and length of the copper tubes were 28, 0.75, and 23 mm, respectively. Steel rods had the radius R_m = 9.24 mm and were single-used in each experiment. The nanopowder was filled in a gap formed by a copper tube and a rod with the usage of a vibrating table. Apparent density of nanopowder, ρ_0, was 0.35 g/cm^3 (about 10% of theoretical density ρ_m). Moreover, to exclude the edge effect on compact density, the mold had a special design. As shown in Fig. 6, the end plugs were installed in the ends of the copper tube and capsulated with plastic washers. Before the MPC the mold was evacuated to residual pressure of 5 Pa and then placed inside an inductor to be compacted. Figure 6 also demonstrates a mold view after the MPC.

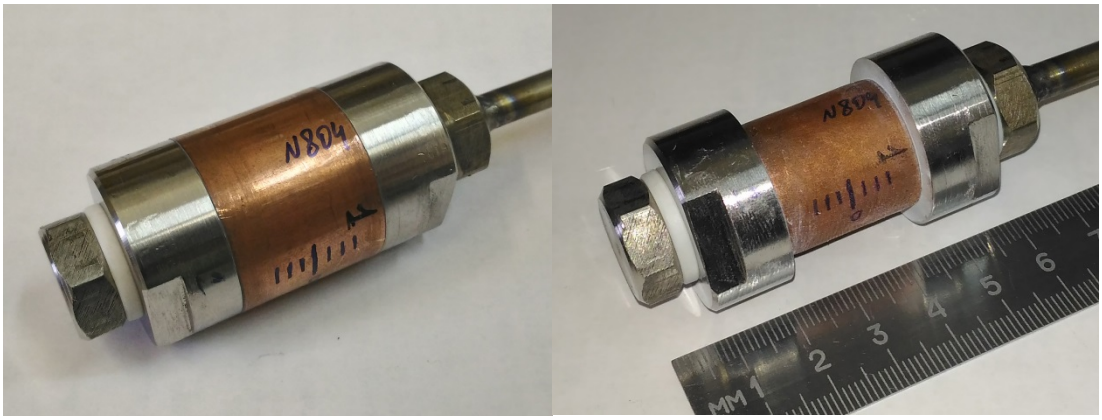

Fig. 6. View of fitted mold (sample No. 804) before (left) and after (right) the MPC

During the experiments the magnetic field applied to the outer surface of the copper tube was carefully measured using a loop inductive probe arranged in a circle in the gap between the inductor and the copper tube. The probe was set in the middle plane of the mold. Typical magnetic field pulses generated by the inductors used are shown in Fig. 7. One can observe that the magnetic system with multi-turn coil is very sensitive to copper shell movement (its radial compression) since it substantially changes the inductance of "inductor – shell" system. In this case the end of the compaction process can be easily determined by the oscillogram. Thus, the shell stop corresponds to a time moment t = 32 μs from the pulse beginning, where a break in the $B_m(t)$ dependence is observed. In experiments with the single-turn coil, a similar effect is not observed, because, firstly, as will be shown below, the shell stops much later than the pulse half-period duration (t = 14 μs), and secondly, the inductor and the external circuit have comparable inductances.

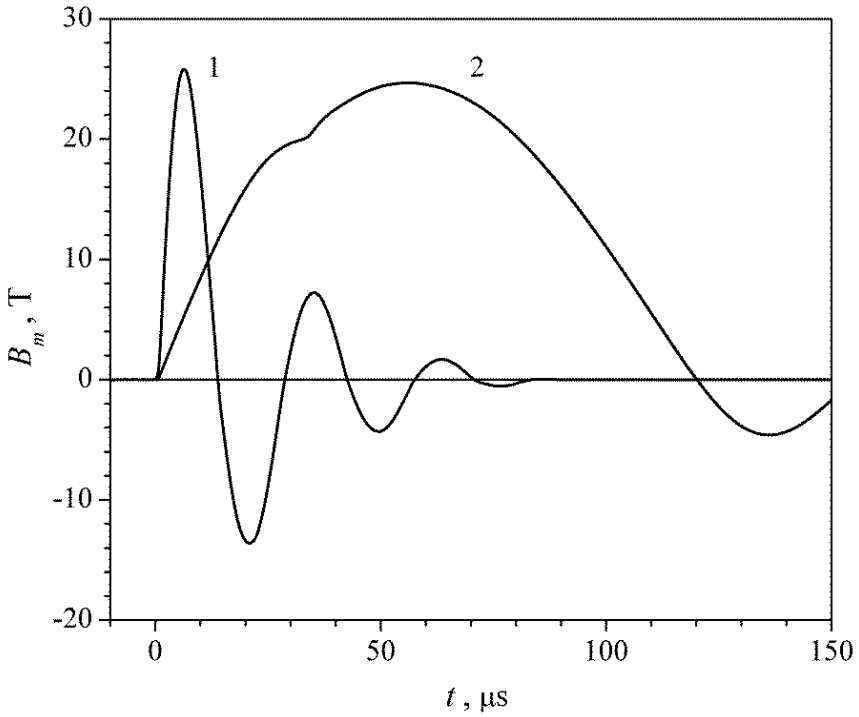

Fig. 7. Time dependence of magnetic field generated by single-turn (curve 1) and multi-turn (curve 2) coils

Characteristics of compact samples obtained are listed in Table 1. It can be seen that the usage of a longer field pulse (inductor 2 case) makes it possible to use magnetic energy more efficiently and to obtain a higher density of the compact.

Table 1. Sample characteristics: D_{end} is the outer diameter of a copper tube after the compression, ρ_0 and ρ_{end} are the starting and the final density of a compact; B_m is the magnetic field amplitude

Inductor	No.	D_{end}, mm	ρ_0, g/cm^3	ρ_{end}, g/cm^3	B_m, T
1	807	22.0±0.3	0.35	2.00	25.9
	808	22.1±0.3	0.35	1.90	25.8
	809	21.9±0.2	0.36	2.20	25.8
2	804	21.6±0.1	0.33	2.70	24.3
	805	21.7±0.1	0.34	2.53	24.7
	806	21.6±0.1	0.34	2.77	23.6

A theoretical analysis of the performed experiments and the data obtained was carried out within the framework of the θ-pinch pressing model described in detail in [2,23,24]. Dynamics of compaction of experimental samples, "powder + shell", is characterized in Fig. 8 by the time dependencies of the velocity of an inner surface of conductive shell, $v_d = dR_d / dt$ (R_d – the inner radius of the shell), when pressed using the inductors 1 and 2. It is interesting to note here that an order of magnitude faster loading, which is realized when the single-turn coil (inductor 1) is used, does not lead to a corresponding increase in the shell velocity. For both inductors used, the velocity v_d is approximately the same by the amplitude and is about 240 m/s. Thus, in conditions of relatively fast loading, the dynamics of the deformable

system, "powder + shell", is primarily determined by the inertial properties of the sample itself, rather than time characteristics of an external pressure pulse [2].

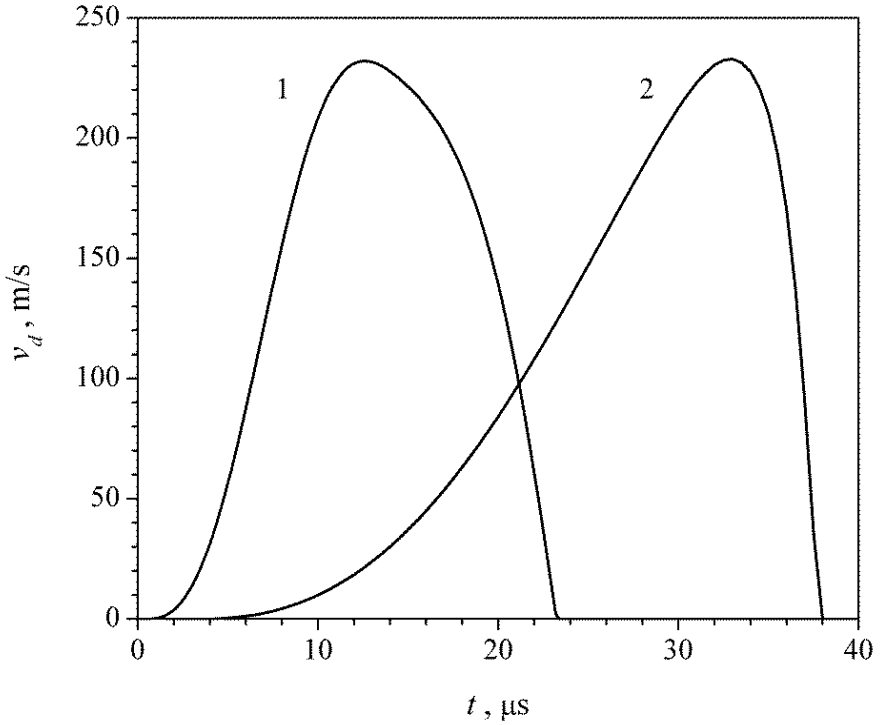

Fig. 8. The velocity of the inner shell surface when compressed by the inductor 1 (curve 1) and the inductor 2 (curve 2)

For the shorter pulse (inductor 1 case), the main accelerating effect is exerted by the first half-wave of magnetic field pulse (at an amplitude of about 25 T) which was about 14 μs. The amplitude of the second half-wave (see Fig. 7) is already half as low, and the "magnetic pressure", $p_m = B^2/(2\mu_0)$, developed at the same time is correspondingly reduced by a factor of four. In the theoretical calculation, the elimination of the second and subsequent half-waves practically does not affect the dynamics of the deformed system and the final density of the compact. At the same time, as shown in Fig. 8, the pressing process in the inductor 1 has not yet been completed to the end of the first half-period of the accelerating pulse. The compression of the shell and the compaction of the powder continue after the end of the external pulse, up to the instant time $t = 23$ μs. At this stage, the deformation of the mechanical system "powder + shell" occurs not under the action of external pressure, but "by inertia", i.e. due to stored kinetic energy. In this case, the pressure realized in the compacted powder can significantly exceed the initial "magnetic" pressure p_m which is about 250 MPa for magnetic field of 25 T in amplitude. According to the calculations the pressure realized by the inertial effect in the powder being compacted reaches 450 MPa. Usage of a longer pulse (inductor 2 case), as noted above, makes it possible to use the energy of the magnetic field even more efficiently. Calculations show that in this case the pressure in the powder reaches about 1.3 GPa, i.e. it exceeds more than 5 times the amplitude of the external pulse.

Despite the approximate equality of the amplitudes of the shell velocities, v_d, as is seen from Fig. 8, the powder compaction rate,

$$v_\rho = \frac{-1}{\rho}\frac{d\rho}{dt} = \frac{2R_d v_d}{R_d^2 - R_m^2}, \tag{11}$$

differs significantly when pressed using the inductors 1 and 2. If one use a shorter pulse (inductor 1), the shell velocity, v_d, reaches its maximum at a thickness of the powder layer $R_d - R_m \cong 1.4$ mm that gives $v_\rho \cong 0.13$ μs^{-1}. For a longer pulse (inductor 2), the same conditions realize at $R_d - R_m \cong 0.9$ and $v_\rho \cong 0.23$ μs^{-1}, respectively. Thus, contrary to the relatively slow loading of the deformable mechanical system "powder + shell" when using the inductor 2, a faster powder compaction process is realized here, and as a consequence, the influence of the "viscous" term in Eq. (10) should be more significant.

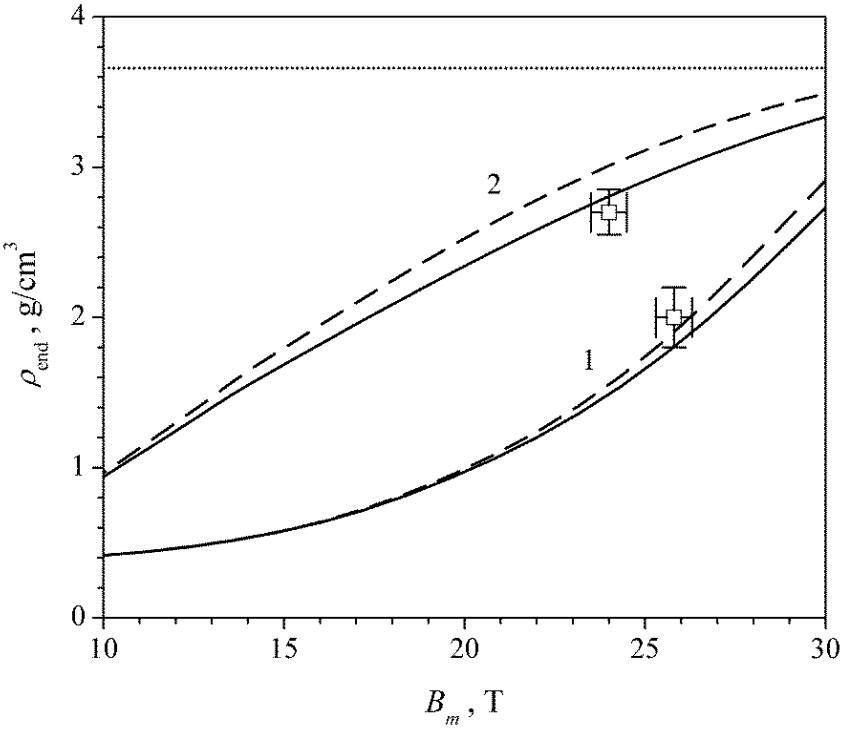

Fig. 9. The final compact density as a function of magnetic field amplitude when pressed using the inductors 1 and 2. The points correspond to the experimental data (see Table 1). The solid lines are the theoretical calculation taking into account the "viscous" term in the powder densification curve (10); dashed lines are the case, when the "viscous" term is off, i.e. $p(\rho) = p_{stat}(\rho)$. The dotted line is the theoretical density level

The influence of the "viscous" term in Eq. (10) on the values of the achieved compact density, ρ_{end}, is demonstrated in Fig. 9. The calculations are performed in the range of the magnetic field amplitudes from 10 to 30 T. The experimental points in the Fig. 9 correspond to the averaged data from Table 1. The dashed lines demonstrate a theoretical calculation in the quasistatic approximation, $p(\rho) = p_{stat}(\rho)$, when the coefficient k_v in Eq. (10) is assumed to be zero. The figure shows that taking into account the "viscous" term with the value of the coefficient k_v obtained in the framework of modeling by the method of granular dynamics makes it possible to improve the agreement of the theoretical model [2,23,24] and the experimental data obtained on the MPC of nanopowder in the θ-pinch mode. First of all this refers to a faster process, i.e. when using an inductor 2. At the amplitude of the magnetic field of 24 T, taking into account the influence of the compaction rate leads to a decrease in the value of the reached final density of the compact, ρ_{end}, from 2.99 g/cm^3, which is much higher than the experimental data, to 2.79 g/cm^3. For a relatively slow compaction process

(inductor 1 case), the effect of the compaction rate decreases and leads to a shift in the values of ρ_{end} from 1.93 g/cm^3 to 1.83 g/cm^3.

5. Conclusion

For the first time, the influence of the compression rate on the compactibility of oxide nanopowders has been studied by a three-dimensional granular dynamics method. Processes of stress relaxation after the stage of high-speed compression with the strain rates of $10^7 – 10^{10}$ s^{-1} up to the relative density $\rho \cong 0.75$ have been analyzed. In particular, it has been found that the characteristic time of the stress relaxation is about 18 ns. The explicit dependence of the compaction pressure, which is connected with the yield strength within phenomenology of powder body [1,2], on the strain rate has been established. It turns out that the rate dependence of pressure is not depending on the compaction conditions (the uniform or the uniaxial pressing). It has been found that nanosized powders demonstrate the power-law dependence of pressure on strain rate: $p \propto v^{1/8}$. In view of small value of the index (0.125) the rate dependence obtained is in general agreement with plastic flow of solid bodies (metals), where the yield strength is proportional to the logarithm of the strain rate [13]. The strain rate dependence of the compaction pressure obtained in the framework of the granular dynamics was used to interpret the experimental data on high-speed compaction of alumina nanopowder (strain rate is about 0.1 μs^{-1}). It is shown that taking into account the strain rate factor makes it possible to improve the agreement between theory and experimental data on the magnetic pulsed compaction of nanopowder.

Acknowledgements. *The authors are indebted to Dr. I.V. Beketov and Dr. A.I. Medvedev for supplying us with alumina nanopowders and performing the powders certification. The work has been supported in part by RFBR (project No. 16-08-00277).*

References

[1] Shtern MB, Serdyuk GG, Maksimenko LA, Truhan YV, Shulyakov YM. *Phenomenological Theories of Powder Pressing.* Kiev: Naukova Dumka; 1982. (In Russian)

[2] Boltachev GS, Nagayev KA, Paranin SN, Spirin AV, Volkov NB. *Magnetic Pulsed Compaction of Nanosized Powders*. New York: Nova Science Publishers, Inc.; 2010.

[3] Filonenko VP, Khvostantsev LG, Bagramov RK, Trusov LI, Novikov VI. Compacting tungsten powders with varying particle size using hydrostatic pressure up to 5 GPa. *Powder Metall. Met. Ceram*. 1992;31(4): 296-299.

[4] Ushakov AV, Karpov IV, Lepeshev AA, Fedorov LY. Copper Oxide of Plasma-Chemical Synthesis for Doping Superconducting Materials. *Int. J. Nanosci*. 2017;16(4): 1750001.

[5] Olevsky EA, Bokov AA, Boltachev GS, Volkov NB, Zayats SV, Ilyina AM, Nozdrin AA, Paranin SN. Modeling and optimization of uniaxial magnetic pulse compaction of nanopowders. *Acta Mech*. 2013;224(12): 3177-3195.

[6] Boltachev GS, Lukyashin KE, Shitov VA, Volkov NB. Three-dimensional simulations of nanopowder compaction processes by granular dynamics method. *Phys. Rev. E*. 2013;88(1): 012209.

[7] Boltachev GS, Volkov NB, Kochurin EA, Maximenko AL, Shtern MB, Kirkova EG. Simulation of the macromechanical behavior of oxide nanopowders during compaction processes. *Granul. Matter*. 2015;17(3): 345-358.

[8] Kotov YA. Electric Explosion of Wires as a Method for Preparation of Nanopowders. *J. Nanopart. Res*. 2003;5(5-6): 539-550.

[9] Kaygorodov AS, Ivanov VV, Khrustov VR, Kotov YA, Medvedev AI, Osipov VV, Ivanov MG, Orlov AN, Murzakaev AM. Fabrication of Nd:Y_2O_3 transparent ceramics by

pulsed compaction and sintering of weakly agglomerated nanopowders. *J. Eur. Ceram. Soc*. 2007;27(2-3): 1165-1169.
[10] Agnolin I, Roux JN. Internal states of model isotropic granular packings. I. Assembling process, geometry, and contact networks. *Phys. Rev. E*. 2007;76: 061302.
[11] Gilabert FA, Roux JN, Castellanos A. Computer simulation of model cohesive powders: Plastic consolidation, structural changes, and elasticity under isotropic loads. *Phys. Rev. E*. 2008;78: 031305.
[12] Regel' VR, Slutsker AI, Tomashevskii EE. The kinetic nature of the strength of solids. *Sov. Phys. Usp*. 1972;15: 45-65.
[13] Vasin RA, Lensky VS, Lensky EV. *Problems of the dynamics of elastic-plastic continuum*. *Chapter 7*. Moscow: Mir; 1975.
[14] Belan VG, Durmanov ST, Ivanov IA, Levashov VF, Podkovyrov VL. Energy loss by plastic deformation in radial compression of a cylindrical shell. *J. Appl. Mech. Tech. Phys*. 1983;24(2): 236-242.
[15] Allen MP, Tildesley DJ. *Computer Simulation of Liquids*. Oxford: University Press; 2003.
[16] Boltachev GS, Volkov NB, Kaygorodov AS, Loznukho VP. The Peculiarities of Uniaxial Quasistatic Compaction of Oxide Nanopowders. *Nanotechnologies in Russia*. 2011;6(9-10): 639-646.
[17] Brilliantov NV, Spahn F, Hertzsch JM, Pöschel T. Model for collisions in granular gases. *Phys. Rev. E*. 1996;53(5): 5382-5392.
[18] Brilliantov NV, Pöschel T. *Kinetic Theory of Granular Gases*. Oxford: University Press; 2004.
[19] Boltachev GS, Spirin AV, Chingina EA. Simulation of high-speed compaction processes of nanopowders by 2D granular dynamics method. *Proc. XVII All-Russian school-seminar on condensed matter problems (SPFKS-17)*. Ekaterinburg: IMP UB RAS; 2016. p. 185. (In Russian)
[20] Landau LD, Lifshitz EM. *Theory of Elasticity*. Oxford: Pergamon Press; 1993.
[21] Grigoriev IS, Meilikhov EZ. (eds.) *Physical Quantities: Handbook*. Moscow: Energoatomizdat; 1991. (In Russian)
[22] Petrov YV, Borodin EN. Relaxation mechanism of plastic deformation and its justification using the example of the sharp yield point phenomenon in whiskers. *Phys. Solid State*. 2015;57(2): 353-359.
[23] Boltachev GS, Volkov NB, Paranin SN, Spirin AV. Dynamics of Cylindrical Conducting Shells in a Pulsed Longitudinal Magnetic Field. *Technical Physics*. 2010;55(6): 753-761.
[24] Boltachev GS, Volkov NB, Chingina EA. Nanopowders in Dynamic Magnetic Pulse Compaction Processes. *Nanotechnologies in Russia*. 2014;9(11-12): 650-659.